JGR Solid Earth

Key Points:

- 3D coupled thermo-mechanical-landscape evolution models show development of offset continental rift basins
- Models show five styles of rift linkage depending on rift offset, crustal rheology, and surface process efficiency
- The 3D models explain characteristic features of offset rift basins observed in the East African Rift system

Author Contributions:

Conceptualization: Lorenz Wolf, Ritske S. Huismans, Sebastian G. Wolf, Delphine Rouby
Formal analysis: Lorenz Wolf, Ritske S. Huismans, Sebastian G. Wolf
Funding acquisition: Ritske S. Huismans, Delphine Rouby
Investigation: Lorenz Wolf, Ritske S. Huismans, Sebastian G. Wolf
Methodology: Sebastian G. Wolf, Dave A. May

Evolution of Rift Architecture and Fault Linkage During Continental Rifting: Investigating the Effects of Tectonics and Surface Processes Using Lithosphere-Scale 3D Coupled Numerical Models

**Lorenz Wolf[1]** , **Ritske S. Huismans[1]** , **Sebastian G. Wolf[1]** , **Delphine Rouby[2]** , and **Dave A. May[3]**

[1]Department of Earth Science, Bergen University, Bergen, Norway, [2]Géosciences Environnement Toulouse, UMR5563 CNRS–IRD–Université de Toulouse, Toulouse, France, [3]Scripps Institution of Oceanography, University of California San Diego, La Jolla, CA, USA

Abstract Continental rifts grow by propagation, overlap and linkage of individual fault segments. These processes are influenced by erosion and sedimentation and generate complex three-dimensional fault-interaction patterns. We use a 3D thermo-mechanical model of lithosphere deformation coupled with surface processes to investigate the coupling between erosion and tectonics, fault interaction and rift linkage, and evaluate the respective characteristics of crustal strength, inherited structures and erosional efficiency. We find that (a) weaker crust limits interactions between individual rift segments, (b) inherited structures are a major control for fault overlap and linkage except if they are too far apart and prevent interaction, and (c) efficient surface processes prolong fault activity, increase accommodated offset and in doing so, limit fault segment propagation and interactions. From these individual feedbacks, we identify five types of characteristic rift architectures: (a) for strong crust and intermediate erosional efficiency, fault segments link and form a horst between the propagating rifts. (b) Decreasing notch offset leads to segmentation of the central horst. (c) In case of reduced crustal strength no fault linkage occurs and a continuous central horst is promoted. (d) If inherited structures are too far apart, irrespective of crustal strength and erosional efficiency, rift basins do not link and a wide plateau-like horst forms between the propagating rifts. (e) In case of efficient erosion, fault linkage is achieved by the formation of strike-slip faults connecting the individual rift segments. Several of these simulated rift architectures can be identified in the western branch of the East African Rift.

Plain Language Summary Continental rifting occurs as a response to extensional, tectonic forces. As a consequence, rifts extending over tens to hundreds of kilometers and consisting of subsided basins and high-elevation rift shoulders are formed at the surface of the Earth. These rifts consist of individual rift segments that interact with each other during the million-year long evolution of the rifts, resulting in a complex rift architecture. What impacts rift segment interaction is widely disputed, and here we use a 3D computer model to investigate the evolving rift architecture between two rift segments. We see that the mechanical strength of the Earth's crust, preexisting structures and the efficiency of erosion at the surface of the Earth have a strong impact on rift segment interaction. Depending on the feedback between these three factors, we observe five characteristic patterns of rift architecture showing variable degrees of interaction and linkage between the individual rift segments. As a particular case, we observe rift linkage through the formation of strike-slip faults for very efficient erosion in our simulations. Moving from simulations to natural examples of rifting, several of our simulated architectures can be identified in the western branch of the East African Rift System.

1. Introduction

Continental rifts form in response to extending lithosphere. As a consequence, subsided basins flanked by border faults and high-relief rift shoulders are visible at the Earth's surface, extending along-strike over tens to hundreds of kilometers. The high-relief rift shoulders erode and generate sediments that are deposited in the surrounding basins. Rifts are commonly segmented and individual border faults propagate, overlap, and interact with each other with ongoing extension (Ebinger, 1989; McConnell, 1972; Morley et al., 1990; Manighetti et al., 1997, 1998, 2001; Morley, 2002, 2010; Rosendahl, 1987). This leads to complex patterns of faulting in the transfer zones and to a variable rift architecture along-strike. In some cases with large rift offset the individual

Project Administration: Ritske S. Huismans

Resources: Ritske S. Huismans

Software: Ritske S. Huismans, Sebastian G. Wolf, Dave A. May

Supervision: Ritske S. Huismans

Validation: Lorenz Wolf, Ritske S. Huismans, Sebastian G. Wolf

Visualization: Lorenz Wolf, Sebastian G. Wolf

Writing – original draft: Lorenz Wolf, Ritske S. Huismans, Sebastian G. Wolf, Delphine Rouby, Dave A. May

Writing – review & editing: Lorenz Wolf, Ritske S. Huismans, Sebastian G. Wolf, Delphine Rouby

rift segments overlap without apparent interaction (Gawthorpe & Hurst, 1993; Morley et al., 1990). Observations from natural examples of rifting suggest that the locus of individual border faults and rift segments is often influenced by inherited older structures (e.g., Fazlikhani et al., 2017; Heilman et al., 2019; Molnar et al., 2020; Phillips et al., 2019). In addition, it has been shown that the strength of the continental crust control rift width, rift asymmetry, and resulting rift architecture (Bassi et al., 1993; Beucher & Huismans, 2020; Buck, 1991; Corti et al., 2018; Huismans & Beaumont, 2003; Tetreault & Buiter, 2018; Theunissen & Huismans, 2019). The present day active segmented East African Rift System (EARS) serves as good natural analogue of offset rift interaction and exhibits a range of characteristic features. Some rift segments with moderate offset exhibit a change of rift fault polarity and complex horst-like structures in the rift linkage area of variable size. Other rift segments with larger offset appear to exhibit minimal interaction with overlapping rift segments. The controls of this range of rift linkage structures and the relative importance of rift offset and inherited weakness remains unclear.

Research during the past decades has revealed a coupling and feedback between tectonic and surface processes (e.g., Champagnac et al., 2012; Molnar & England, 1990; Whipple, 2009; Whittaker, 2012). Mountain belts have been the particular focus of many studies that identified that orographic precipitation can focus deformation (Beaumont et al., 1992; Enkelmann et al., 2009; Glotzbach et al., 2013; Grujic et al., 2006; Willett, 1999; Zeitler et al., 2001), and that the overall style of orogen deformation is sensitive to erosion and deposition (e.g., Erdős et al., 2015; S. G. Wolf et al., 2021). In continental rifts, footwall erosion and hangingwall deposition provide a feedback and enhance duration and offset of normal faults (Maniatis et al., 2009; Olive et al., 2014), which promotes formation of asymmetric, large offset normal faults (Beucher & Huismans, 2020; Hemelsdaël et al., 2017; Theunissen & Huismans, 2019). Hence, besides the tectonic variables, surface processes controlled by climate strongly impact rift architecture, in particular in terms of localization of deformation and fault offset. Additionally, how individual faults and rift segments link has a strong influence on evolving rift architecture, sediment pathways, and sediment distribution within a rift system (Gawthorpe & Hurst, 1993; Gawthorpe & Leeder, 2000). Understanding the evolution of rift architecture is therefore vital to understand the evolution of the sedimentary record — in particular, if the sediment record of a basin is used to deduce tectonic or climatic signals (e.g., Hodgson et al., 2018; Straub et al., 2020).

Progress in the development of high performance computing facilitated the emergence of efficient 3D-thermo-mechanical codes in the past decade (e.g., Braun et al., 2008; Thieulot, 2011; May et al., 2014). These and other codes have been applied in a series of subsequent studies investigating rifting processes, focusing on fault linkage using crustal scale models (Allken et al., 2011, 2012), rift heterogeneity as a consequence of fault evolution (Naliboff et al., 2020), the effects of oblique rifting (e.g., Duclaux et al., 2020; Jourdon et al., 2020; Le Pourhiet et al., 2017), the effects of variations in crustal rheology (Brune et al., 2017; Gouiza & Naliboff, 2021), or the role played by structural inheritance (e.g., Balázs et al., 2018; Dunbar & Sawyer, 1996; Glerum et al., 2020; Heron et al., 2019; Katzman et al., 1995; Neuharth et al., 2021). Only few of these studies include surface processes. Here, we simulate the evolution of continental rifts in 3D subject to different tectonic and climatic boundary conditions. We use a high-resolution 3D-thermo-mechanical model coupled to a landscape evolution model to investigate the interaction of continental rifting and surface processes. We focus on particular on understanding how fault linkage is affected by tectonic and surface processes.

The model setup allows for the development of two individual rift segments that propagate and possibly link during extension. We analyze how faults between the two rift segments interact and link with each other and how the resulting rift architecture varies between the models. We test the sensitivity of our setup to variable crustal rheology, style of structural inheritance and fluvial erodibility in a series of 12 models, and identify five rift architectures characteristic of specific climatic and tectonic conditions. The idea with our model, which is one of the first models using a 3D coupled thermo-mechanical-surface process model, is to start with a rather simple setup and model geometry (e.g., uniform extension direction and rate, inherited structures), and to focus on the early stages of continental rifting. Hence, the comparison with natural systems is only reasonable for rifts that have good data coverage, are currently active and in their early stages and that reflect our considered model setup. Considering these criteria leaves only a limited number of present-day continental rift systems and we picked the central segment of the EARS around Lake Tanganyika to which we compare our models.
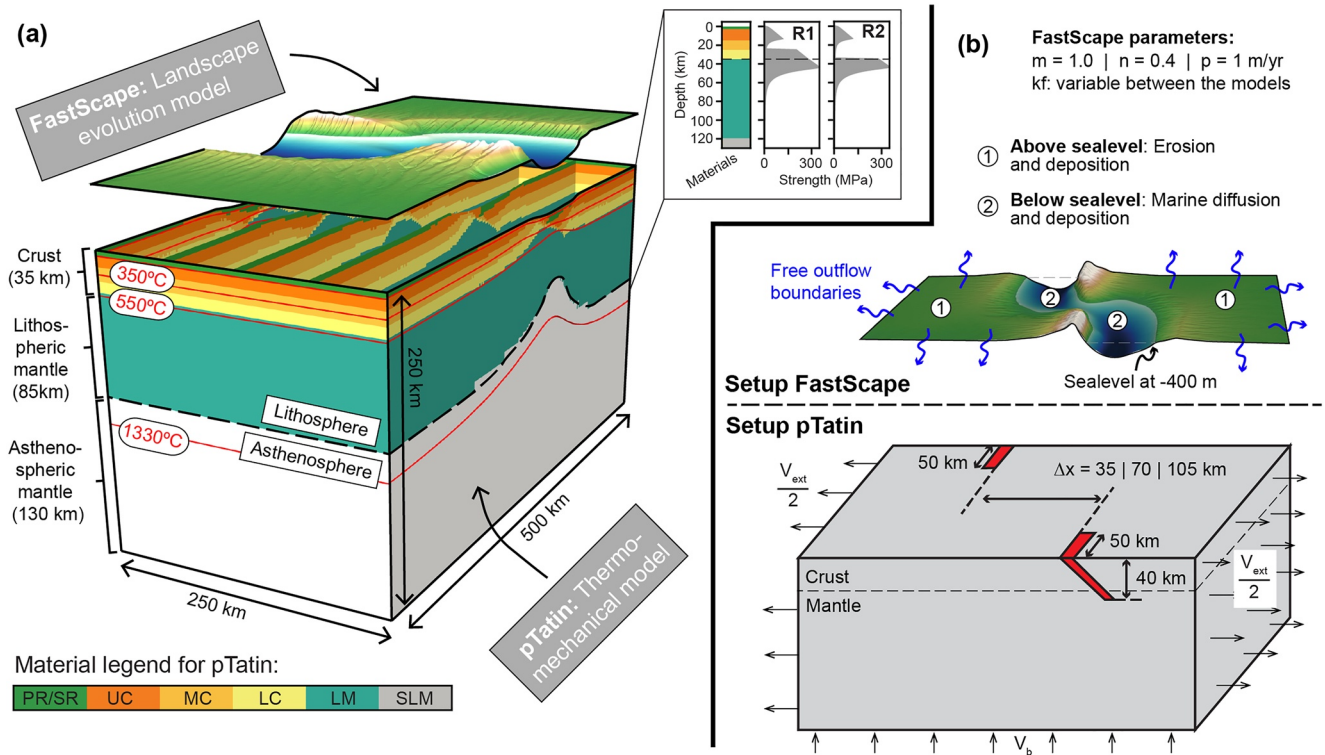
Figure 1. Overview of the coupled model setup: (a) pTatin (thermo-mechanical model) is coupled with FastScape (surface process model). The pTatin model is vertically stratified and the crust consists of pre-rift/syn-rift sediments (PR/SR), upper crust (UC), middle crust (MC) and lower crust (LC). The mantle is subdivided in lithospheric mantle (LM) and sublithospheric mantle (SLM). (b) Setup for FastScape (top) and pTatin (bottom). For FastScape, we use a constant precipitation rate (*p*) and stream power exponents (*m* and *n*), but vary the fluvial erodibility (*k_f*). For pTatin, we use two oppositely-dipping notches at the model front and back to aid initial strain localization. We vary the notch offset (Δ*x*). *v_ext* is the extension rate, and *v_b* the bottom inflow. We tested two rheologies (R1 and R2) with different strength of the lower crust (see inset).

2. Methods

2.1. pTatin

To simulate long-term extension of the lithosphere and rift formation in 3D, we use the Arbitrary Lagrangian-Eulerian (ALE) finite element code pTatin (May et al., 2014; May et al., 2015), which solves for the conservation of momentum (1), mass (2), and energy (3):

$$\nabla \cdot (2\eta\dot{\epsilon}) - \nabla P = \rho \boldsymbol{g}, \tag{1}$$

$$\nabla \cdot \boldsymbol{v} = 0, \tag{2}$$

$$c_p\rho \left(\frac{\partial T}{\partial t} + \boldsymbol{v} \cdot \nabla T \right) = \nabla \cdot (k\nabla T) + H + v_z\alpha g_z T \rho, \tag{3}$$

where η is the viscosity, $\dot{\epsilon}$ is the strain rate tensor, P the pressure, ρ the density, $\boldsymbol{g}$ the gravitational vector, $\boldsymbol{v} = (v_x, v_y, v_z)$ is the velocity (v_z corresponds to the velocity in the vertical direction), c_p the heat capacity, T the temperature, t is time, k is the thermal conductivity, H the heat production rate (due to radioactive decay), and α is the thermal expansion coefficient. Density varies as a function of temperature, according to

$$\rho(T) = \rho_0 \left(1 - \alpha \left(T - T_0 \right) \right), \tag{4}$$

where ρ_0 corresponds to the density at temperature T_0.

The model domain is vertically stratified and consists of different materials (Figure 1a), which follow frictional-plastic or non-linear temperature dependent viscous rheologies. Frictional-plastic behavior is modeled with a pressure dependent Drucker-Prager yield criterion

$$\tau_Y = C\cos(\phi) + P\sin(\phi), \tag{5}$$

where ϕ is the internal angle of friction, and C is the cohesion. Material failure occurs whenever

$$\sigma'_{II} > \tau_Y, \tag{6}$$

where σ'_{II} is the square root of the second invariant of the deviatoric stress tensor. Material damage ($\epsilon_{plastic}$) is modeled via the accumulated plastic strain ($\epsilon_{plastic}$), which evolves according to

$$\frac{D\epsilon_{plastic}}{Dt} = \begin{cases} \dot{\epsilon}_{II} & \text{if } \sigma'_{II} > \tau_Y, \\ 0 & \text{otherwise,} \end{cases} \tag{7}$$

where D/Dt denotes the material derivative and $\dot{\epsilon}_{II}$ is the square root of the second invariant of $\dot{\epsilon}$. We include the effects of strain weakening (Huismans & Beaumont, 2003), by linearly decreasing the friction angle from 20° to 4°, and the cohesion from 15 to 2 MPa over a defined strain interval of $0.08 < \epsilon_{plastic} < 0.33$.

Viscous flow is modeled with a temperature-dependent, power-law rheology of the shape:

$$\sigma'_{visc} = f\, A_c^{\frac{-1}{n_c}}\, (\epsilon_{II})^{\frac{1}{n_c}} \exp\left(\frac{Q + VP}{n_c RT}\right) \tag{8}$$

where σ'_{visc} is the square root of the second invariant of the deviatoric stress, f the scaling factor, A_c the pre-exponential factor converted to plane strain, n_c the power-law exponent, Q the activation energy, $V = 0$ activation volume, and R the universal gas constant. To account for the rheological stratification of the model domain, we apply well-established flow laws of wet quartz (Gleason & Tullis, 1995), Dry Maryland Diabase (Mackwell et al., 1998) and wet olivine (Karato & Wu, 1993), and use the scaling factor (f) to vary the strength of crust.

2.2. FastScape

In order to include the effects of surface processes on the tectonic evolution (and vice versa), we couple pTatin with a modified version of the earth surface process model FastScape (Braun & Willett, 2013; Yuan, Braun, Guerit, Rouby, & Cordonnier, 2019; Yuan, Braun, Guerit, Simon, et al., 2019) that accounts both for continental erosion and deposition as well as transport and deposition below sea-level (Figure 1b).

In parts of the model domain above sea-level (h_{sl}), erosion includes fluvial incision as approximated with the extended stream power law (Whipple & Tucker, 1999; Yuan, Braun, Guerit, Rouby, & Cordonnier, 2019) and hill slope processes (Culling, 1963). The rate of change of elevation ($\partial h/\partial t$) corresponds to

$$\frac{\partial h}{\partial t} = U - k_f p^m A^m S^n + k_c \nabla^2 h, +\frac{G}{pA}\int_A \left(U - \frac{\partial h}{\partial t}\right) dA, \text{ if } h \geq h_{sl} \tag{9}$$

where U is the rock uplift rate, k_f is the fluvial erodibility, p is the precipitation rate, A is the upstream catchment area, S is the slope, m and n are the stream power exponents, and k_c is the transport coefficient for hill slope diffusion, G is a non-dimensional continental deposition coefficient, and p is the precipitation rate. We also account for mass-conserving filling of local minima according to available sediments.

Material excavated in the continental domain is transported by rivers and enters the marine part at the shoreline, where it is transported/deposited by a grain-size dependent coupled diffusion equation with different diffusion coefficients. The rate of topographic change below sea-level is approximated by (Yuan, Braun, Guerit, Simon, et al., 2019):

$$\frac{\partial h}{\partial t} = K_{silt}\nabla\cdot(F\nabla h) + K_{sand}\nabla\cdot((1-F)\nabla h) + Q_{silt} + Q_{sand} \tag{10}$$

where K_i are the marine transport coefficients of sand and silt, F is the silt fraction, and Q_i are the sand and silt fluxes provided by rivers to the shoreline. For simplicity we assume that material arriving at the shoreline has

Table 1
Overview of the Material Parameters

Parameter	Symbol [unit]	PR/SR	UC/MC	LC (R1)	LC (R2)	LM	SLM
Frictional rheology							
Cohesion	C [MPa]	20–4	20–4	20–4	20–4	20–4	20–4
Angle of friction	ϕ [°]	15–2	15–2	15–2	15–2	15–2	15–2
Viscous rheology							
Flow law		WQtz	WQtz	DMD	WQtz	WOl	WOl
Scaling factor	F	1	1	1	1	5	1
Activation energy	Q [kJ mol^{-1}]	223	223	485	223	430	430
Power law exponent	n	4	4	4.7	4	3	3
Material constant	A [Pa^{-n} s^{-1}]	8.57×10^{-28}	8.57×10^{-28}	5.78×10^{-27}	8.57×10^{-28}	1.76×10^{-14}	1.76×10^{-14}
Activation volume	V [m^3 mol^{-1}]	0	0	0	0	1.50×10^{-5}	1.50×10^{-5}
Density parameters							
Density at $T = 273\,°$K	ρ_0 [kg m^{-3}]	2,850	2,850	2,850	2,850	3,265	3,280
Thermal expansion	α [K^{-1}]	3.10×10^{-5}	3.10×10^{-5}	3.10×10^{-5}	3.10×10^{-5}	3.10×10^{-5}	3.10×10^{-5}
Thermal parameters							
Thermal conductivity	k [W m^{-1} K^{-1}]	2.25	2.25	2.25	2.25	2.25	2.25
Heat capacity	c_p [J kg^{-1} K^{-1}]	1000	1000	1000	1000	1000	1000
Heat production rate	H [W m^{-3}]	0.90×10^{-6}	0.90×10^{-6}	0.90×10^{-6}	0.90×10^{-6}		

Note. Material names: PR/SR = Prerift/Synrift sediments, UC/MC = Upper/Middle crust, LC(R1/R2) = Lower crust (Rheology 1/2), LM = Lithospheric mantle, SLM = Sublithospheric mantle.

a silt fraction of 50%, so that $Q_{silt}/Q_{sand} = 1$. We refer to the original publication (Yuan, Braun, Guerit, Simon, et al., 2019) for further details.

FastScape (Figure 1a) receives the velocity field of the free surface from pTatin as input. After each pTatin time-step, the FastScape surface is advected accordingly and the changes in topography are calculated according to Equations (7) and (8). At the end of a FastScape cycle, the updated surface is handed over to pTatin as input for the next timestep of the tectonic model. Hence, both models are two-way coupled, but we do not track the evolution of stratigraphy. Deposited material has the same thermo-mechanical properties as the underlying material, in our models typically the green pre-rift sediments (Figure 1).

2.3. Model Setup and Parameters

The following setup and boundary conditions of pTatin are identical in all models: the models have dimensions of 500 km × 250 km × 250 km (Figure 1a), which together with the chosen model grid resolution (256 × 128 × 64 elements) results in a horizontal resolution of ~2 km. The vertical resolution is depth dependent. The model domain consists of continental crust (35 km thick), lithospheric mantle (85 km thick), and asthenospheric mantle (130 km thick). The top of the model serves as free surface allowing for isostatic adjustment, whereas the front, back, and bottom sides of the model act as free slip boundaries. The left and right sides are extended by half the extension rate $v_{ext}/2$, Figure 1b), which sums up to a total extension rate of 0.5 cm yr^{-1}. In order to preserve mass, material loss on the left and right is counter-balanced with a basal inflow of material (v_b, Figure 1b). We continue extension, until a total amount of 75 km of extension is reached after 15 Ma, which corresponds to continental rifting without full breakup. A single pTatin time step is ~10 kyr long, which provides a good trade-off between numerical stability and computational costs. To initialize localization at discrete structures and investigate different geological situations, we need to include rheological heterogeneities that could originate, for example, from thermal or compositional anomalies, or structures in the crust or mantle inherited from earlier deformation periods. Due to its simplicity and effectiveness, it is a common choice by many scholars, including us, to use strain-weakened notches or seeds to localize deformation and investigate different geological

Table 2
Overview of Surface Process Parameters

Parameter	Symbol [unit]	Value
Fluvial erodibility	k_f [m$^{0.2}$/year]	0.5, 2.5 × 10^{-5}
Hillslope diffusion coefficient	k_c [m^2/year]	1 × 10^{-2}
Stream power law exponent	m	0.4
Stream power law exponent	n	1.0
Precipitation rate	p [m/year]	1
Continental deposition coefficient	G	1
Marine transport coefficient silt	K_{silt} [m^2/year]	200
Marine transport coefficient sand	K_{sand} [m^2/year]	100
Sea level	h_{sl} [m]	−400

scenarios. Following earlier crustal scale 3D modeling of rift linkage (e.g., Allken et al., 2011; Allken et al., 2012), we use two fully strain-weakened ($\epsilon_{plastic} > 0.33$), inclined notches at the model front and back with opposite dip direction that represent two inner offset rift bounding faults and resemble pre-existing inherited structure (Figure 1b). On either side, the weak notches dip by 60° to the left or right and extend to a depth of 40 km. We also show two supplementary models (SM8, SM9, see Supporting Information S1) with simpler strain weakened notches. These models show similar behavior as the models with inclined weak seeds, indicating that the observed model behavior is relatively independent on the shape of the initial notches. Previous model work (e.g., Neuharth et al., 2021) showed that rifting is not very sensitive to notch length. Hence, we only use a single notch length, and each notch extends 50 km into the model domain. The notches are four grid elements wide, which results in a notch width of roughly 8 km.

FastScape has the same dimensions as the tectonic model (500 × 250 km, Figure 1a), and the same number of nodes as the Q2 elements at the upper surface of pTatin, resulting in a mesh resolution of ∼1 km. Each FastScape time step is 500 years long, so that one pTatin time step comprises 20 FastScape time steps. The stream power exponents are set to $m = 0.4$ and $n = 1.0$, respectively, and we use a uniform precipitation rate of $p = 1$ m/yr throughout the entire model domain. We set the sea-level to $h_{sl} = -400$ m (Figure 1b). All four side boundaries are free-outflow boundaries, implying that material transported by rivers to the side boundaries leaves the model.

We test the sensitivity of the setup to varying crustal rheology, rift offset, and fluvial erodibility (see Table 1 for material parameters and Table 2 for surface process parameters). We consider two crustal rheologies (R1 and R2, Figure 1a). R1 uses a Dry Maryland Diabase flow law (Mackwell et al., 1998) for the lower crust, resulting in a mechanically strong crust. R2 uses wet quartz (Gleason & Tullis, 1995) for the lower crust, resulting in an intermediate strength crust. To test the sensitivity of the models to inherited structures, we vary the offset between the strain-weakened notches (35, 70, and 105 km; Figure 1b). Lastly we vary fluvial erodibility (k_f), to account for different erosional efficiencies between the models. In natural systems, k_f has a large variability (e.g., Stock & Montgomery, 1999). We focus on two end member scenarios. A k_f-value of 0.5 × 10^{-5} m$^{0.2}$/yr that equates to an intermediate erodibility and preserves a fluvial landscape (e.g., L. Wolf, Huismans, Rouby, et al., 2022). A k_f-value of 2.5 × 10^{-5} m$^{0.2}$/yr that corresponds to very efficient erosion and results in rapid degradation of the landscape (e.g., S. G. Wolf et al., 2022).

Table 3
Overview of the Parameter Combinations for Our 12 Models

Model name	Rheology	Notch offset [km]	k_f value [m$^{0.2}$/yr]	Displayed in
M1	R1	70	0.50 × 10^{-5}	Figs. 2 + 7
M2	R1	35	0.50 × 10^{-5}	Figs. 3 + 7
M3	R1	105	0.50 × 10^{-5}	Figs. 4 + 7
M4	R1	70	2.50 × 10^{-5}	Figs. 5 + 7
M5	R2	70	0.50 × 10^{-5}	Figs. 6 + 7
SM1	R1	35	2.50 × 10^{-5}	Fig. 7
SM2	R1	105	2.50 × 10^{-5}	Fig. 7
SM3	R2	35	0.50 × 10^{-5}	Fig. 7
SM4	R2	105	0.50 × 10^{-5}	Fig. 7
SM5	R2	35	2.50 × 10^{-5}	Fig. 7
SM6	R2	70	2.50 × 10^{-5}	Fig. 7
SM7	R2	105	2.50 × 10^{-5}	Fig. 7

In total, the parameter combination of two rheologies, three notch-offsets, and two fluvial erodibilities results in 12 different models (Table 3). Five of these (Models M1–M5) are investigated in detail in Figures 2–6. We focus our analysis on Model M1, which serves as a reference model and highlight the differences between the reference model and the respective other models. Animations of model output over the entire model duration can be found as additional files in Supporting Information S1.

3. Results

3.1. The Reference Model M1

The reference model M1 has a high crustal strength (rheology R1), intermediate notch offset (70 km), and a k_f-value of 0.50 × 10^{-5} m$^{0.2}$/yr. The evolution of its topography and structures (5, 10, and 15 Ma) is displayed in Figure 2.

Initial deformation localizes at the two notches at the front and back of the model forming, at 5 Ma, two asymmetric rift segments, ∼60 km wide, with high-relief rift shoulders (∼4 km). Major offset occurs on the inner faults and minor offset on the conjugate faults. The major faults propagate

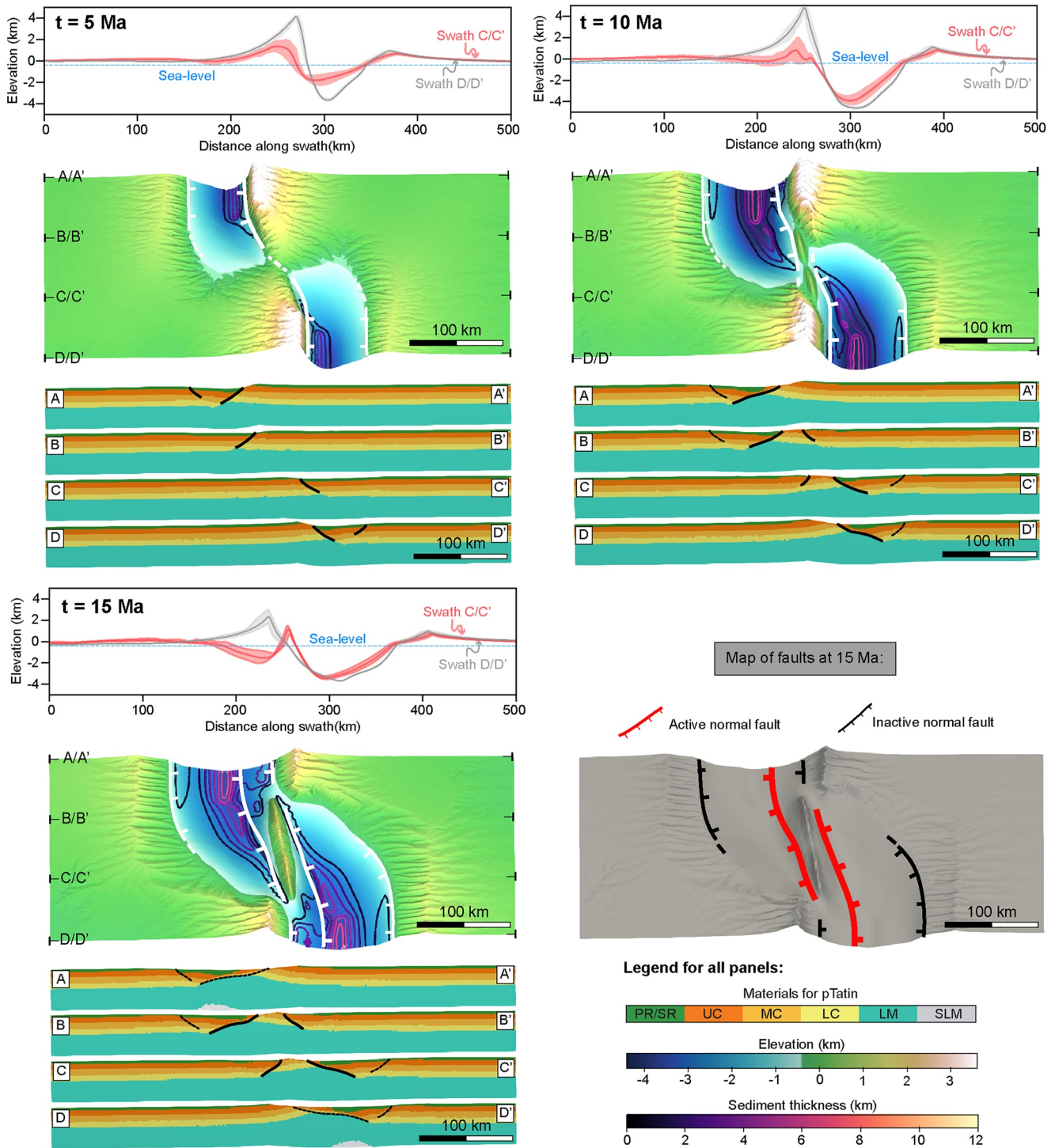**Figure 2.** Evolution of the reference model M1 with high crustal strength (R1), 70 km notch offset and $k_f = 0.50 \times 10^{-5}$ m$^{0.2}$/yr. The model is displayed at 5 Ma, 10 Ma, and 15 Ma. For each time step, two topographic swaths (each 30 km wide), a top-view of the topography and four cross sections (A/A', B/B', C/C', D/D') are provided. A top-view of all faults for the last time step is also displayed.

toward the center of the model and form two separate basins. Along-strike variations in inner fault offset is reflected in the along strike topographic gradient with footwall topography (~4 km high) along the S and N boundary while only ~1.5 km in the center. Highest sediment thickness (~3 km) is located near high-elevation rift shoulders.
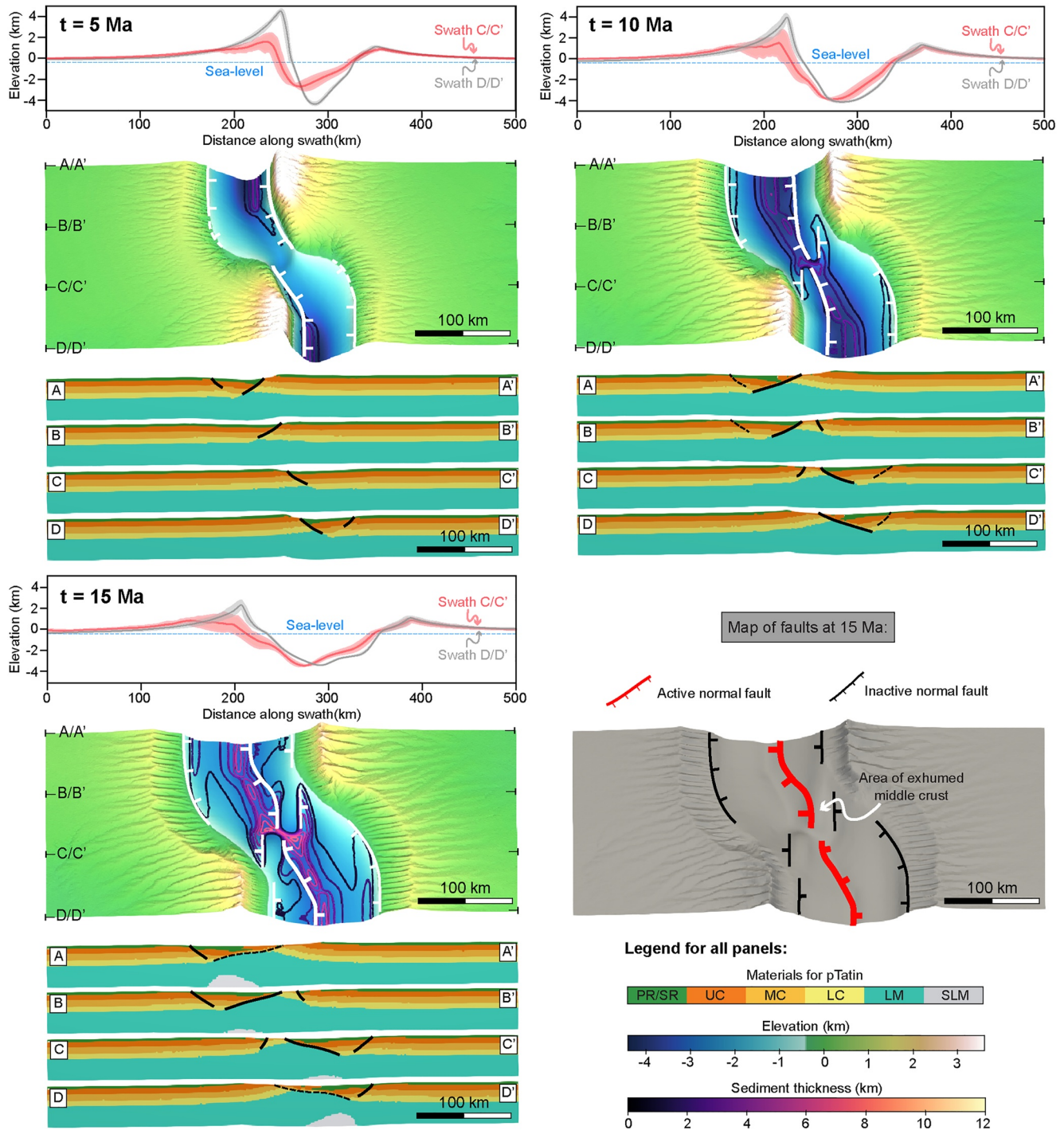
Figure 3. Evolution of model M2 with high crustal strength (R1), 35 km notch offset and a k_f-value of 0.50×10^{-5} m$^{0.2}$/yr. The model is displayed at 5 Ma, 10 Ma, and 15 Ma. For each time step, two topographic swaths (each 30 km wide), a top-view of the topography and four cross sections (A/A', B/B', C/C', D/D') are provided. A top-view of all faults for the last time step is also displayed in the lower right panel.

At 10 Ma, the inner faults reached the center of the model and the rift shoulders ∼5 km in elevation, while the overlapping fault segments form a central horst. The topographic gradient along the rift flanks increases further with ∼5 km elevation on the model boundaries versus ∼1 km in the model center. The thickest depocenter (5 km) is located at the feet of the high-relief rift shoulder with the depocenters propagating toward the center of the model.
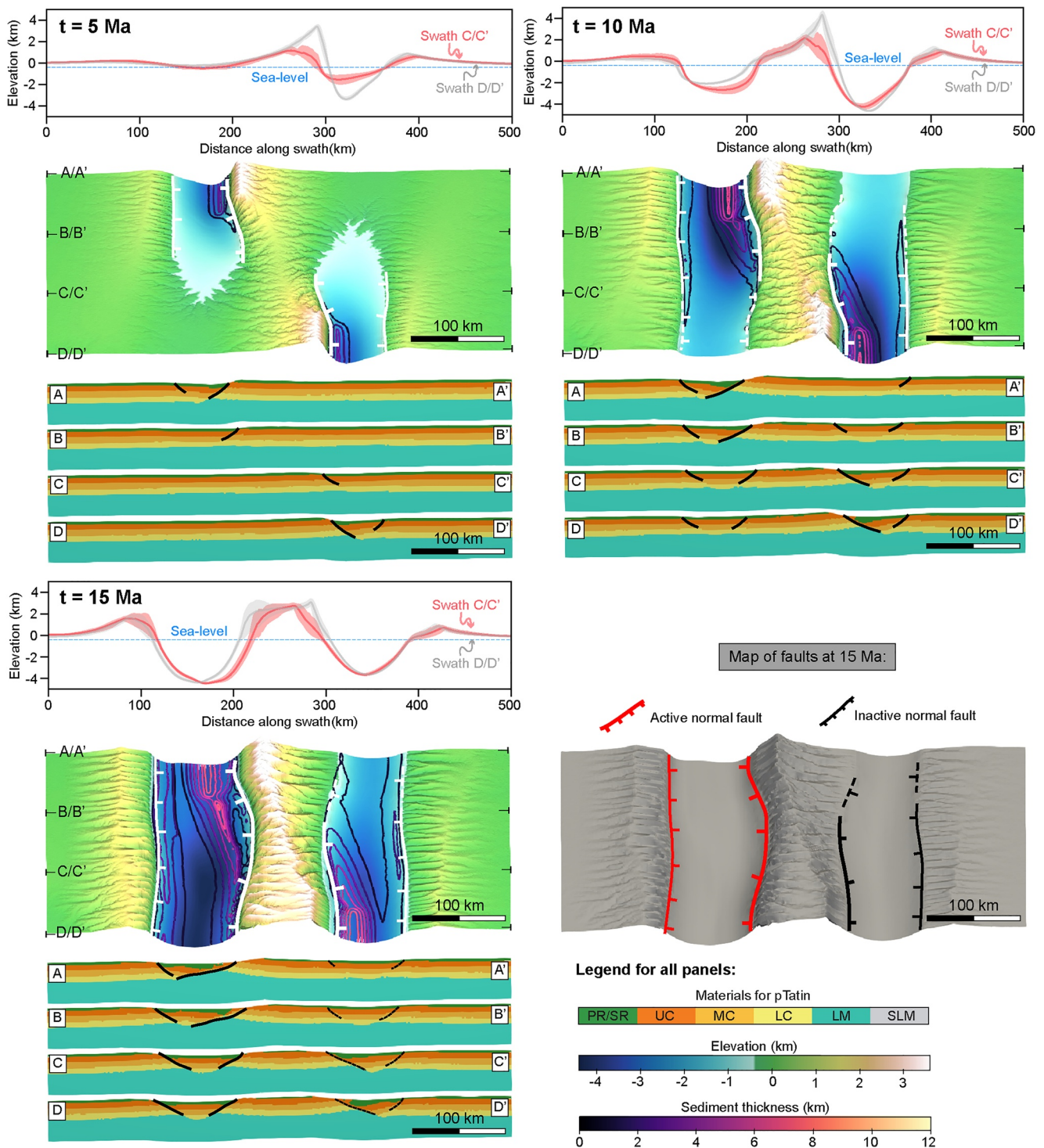
Figure 4. Evolution of model M3 with high crustal strength (R1), 105 km notch offset and a k_f-value of 0.50×10^{-5} m$^{0.2}$/yr. The model is displayed at 5 Ma, 10 Ma, and 15 Ma. For each time step, two topographic swaths (each 30 km wide), a top-view of the topography and four cross sections (A/A', B/B', C/C', D/D') are provided. A top-view of all faults for the last time step is also displayed in the lower right panel.

At 15 Ma, the large offset faults almost completely rupture the crust resulting in two asymmetric rift segments with opposite vergence. In the center of the model, the overlapping faults with opposite dip overlap and border a central horst that separates the two basins. Cessation of uplift on the main inner faults, ongoing erosion, and uplift of the central horst decreases the topographic gradient between the model front/back and center (2.2 vs. 1.5 km).
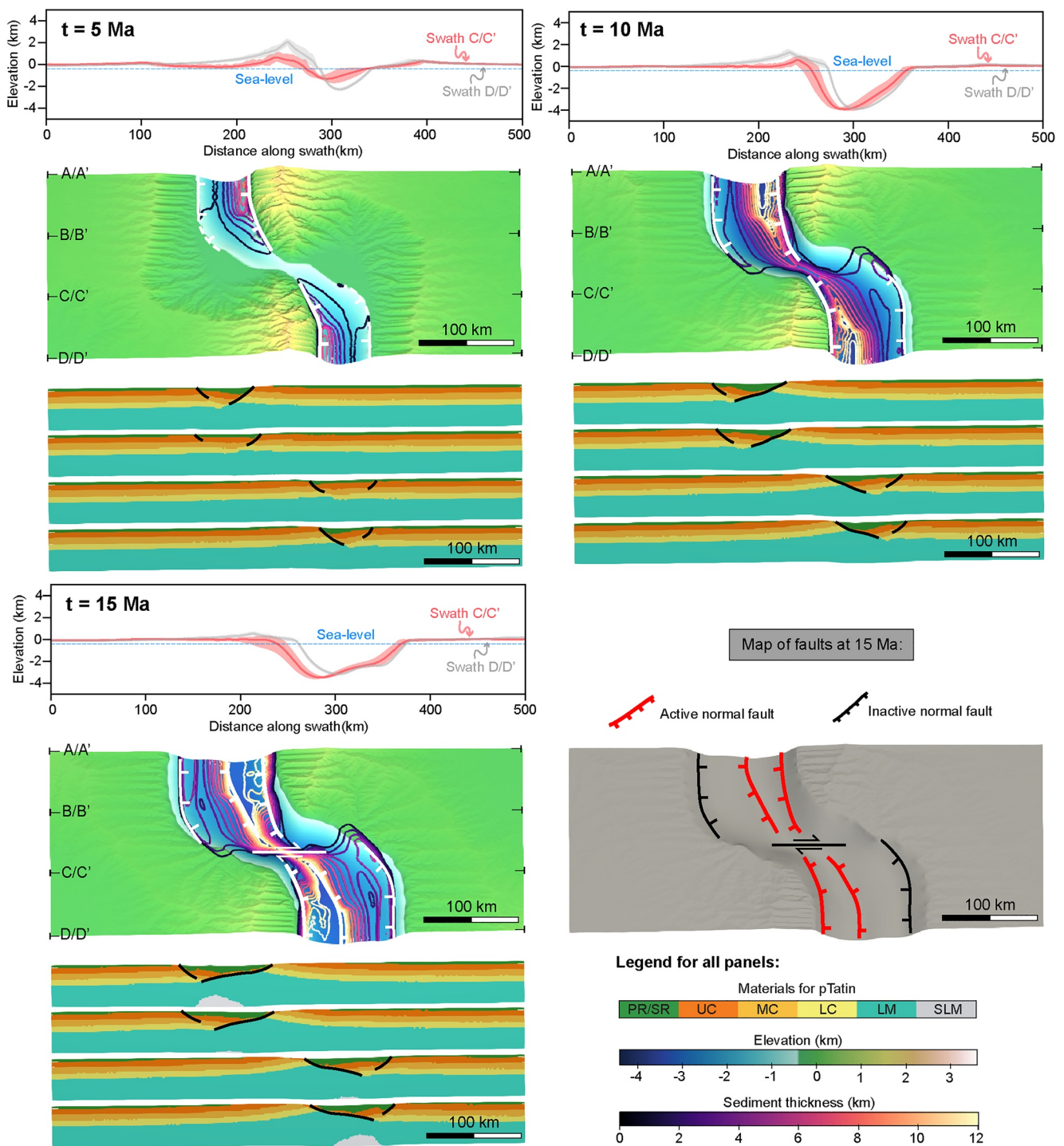
Figure 5. Evolution of model M4 with high crustal strength (R1), 70 km notch offset and a k_f-value of 2.50×10^{-5} m$^{0.2}$/yr. The model is displayed at 5 Ma, 10 Ma, and 15 Ma. For each time step, two topographic swaths (each 30 km wide), a top-view of the topography and four cross sections (A/A', B/B', C/C', D/D') are provided. A top-view of all faults for the last time step is also displayed in the lower right panel.
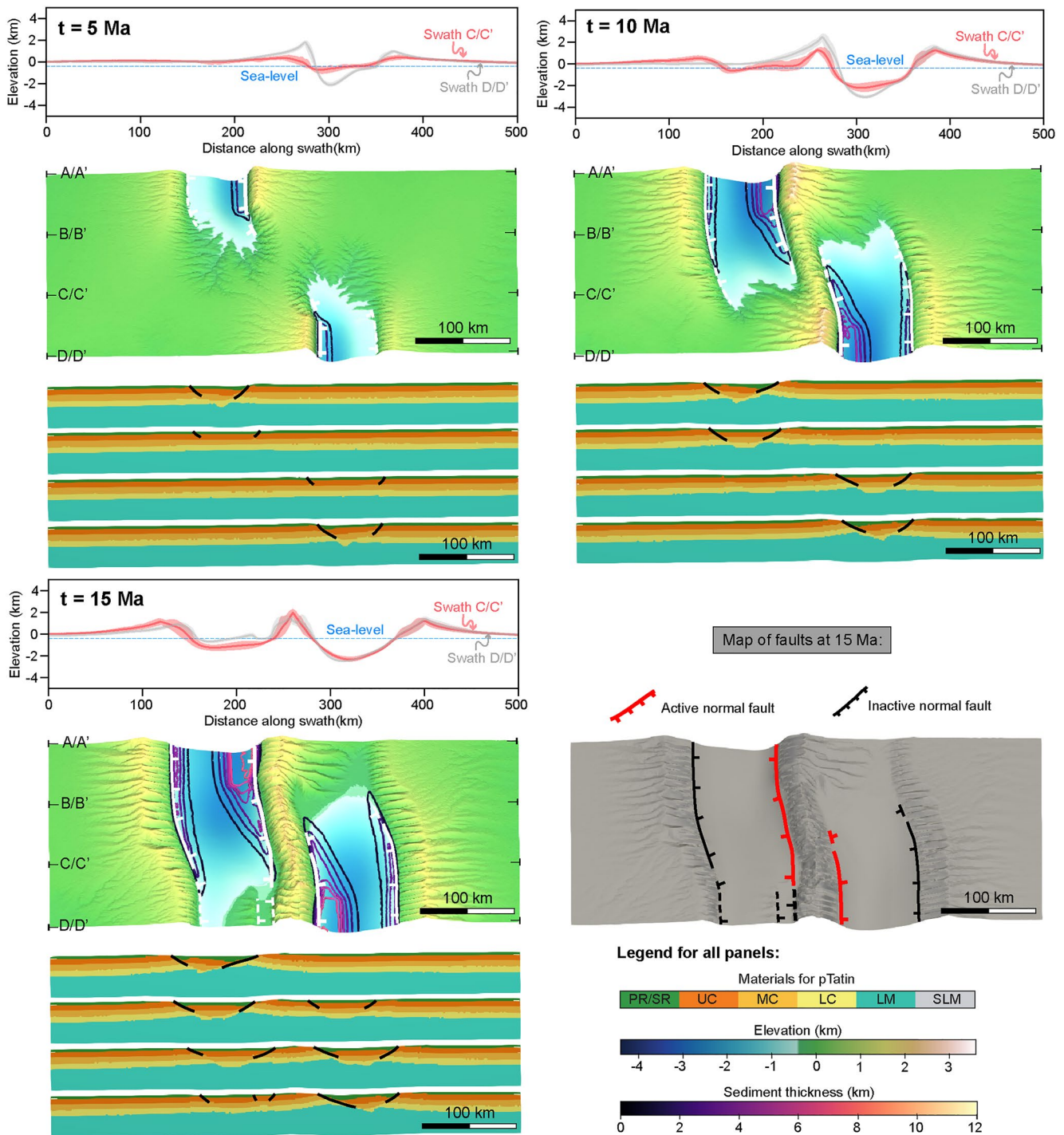
Figure 6. Results for model M5. Evolution of model M5 with intermediate crustal strength (R1), 70 km notch offset and a k_f-value of 0.50×10^{-5} m$^{0.2}$/yr. The model is displayed at time steps of 5 Ma, 10 Ma, and 15 Ma. For each time step, two topographic swaths (each 30 km wide), a top-view of the topography and four cross sections (A/A', B/B', C/C', D/D') of the materials and faults are provided. A top-view of all faults for the last time step is also displayed in the lower right panel.

Erosion of the uplifting central horst increases sediment thickness in the lateral depocenters and maximum sediment thickness (~6 km) is located next to the rift shoulders.

3.2. Effect of Notch Offset: Models M2 and M3

Models M2 (Figure 3) and M3 (Figure 4) have a high crustal strength (R1), a k_f-value of 0.50×10^{-5} m$^{0.2}$/yr, and notch offset is either less (35 km, M2) or more (105 km, M3) than in the reference model (70 km).

Shorter notch offset model M2 produces two small horsts in the central domain where the faults overlap. The horsts never emerge and exhume middle crust. Although two individual rift systems develop, the basins are connected after 4 Myr. The thickest depocenter (7 km) is located in the vicinity of the two horsts.

Larger notch offset model M3 results in two rifts with basins that never connect. The left rift propagates across the model. Hence, after ~12 Ma, the right rift becomes inactive and deformation focuses in the left rift. A continuous horst forms between the two rifts across the model. At the model front, this horst is elevated (~3 km) and 100 km wide. The thickest depocenter (7 km) is located in the left rift.

3.3. Effect of Erosional Efficiency: Model M4

Model M4 (Figure 5) has a high crustal strength (rheology R1), intermediate notch offset (70 km) and a k_f-value of 2.50×10^{-5} m$^{0.2}$/yr, higher than the reference model.

More efficient erosion suppresses the development of a horst between the overlapping major faults. Fault offsets are higher and all faults are active at 15 Ma. At ~14 Ma, a strike-slip fault forms in the linkage zone between the two rift segments. Efficient erosion limits elevation to ~2.5 km and decreases the topographic gradient between model front/back and center. The sediment depocenter is significantly thicker than in the reference model (>12 km).

3.4. Effect of Crustal Strength: Model M5

Model M5 (Figure 6) has an intermediate crustal strength (rheology R2) with otherwise the same parameters as in reference model M1.

Weaker crust results in a different rift style compared to the reference model. Fault offset is lower, more symmetric, and fault propagation is delayed. The major and conjugate faults remain active until 15 Ma and the two rift segments are not linked. A continuous horst forms between the two rifts, connecting the rift shoulders. At 15 Ma, the left rift has propagated across the model domain, forming a continuous basin. At the model front, an additional small conjugate fault dissect the footwall of the left rift. The maximum elevation (~2.5 km) is less than half of what is observed in reference model M1. Formation of the horst and continuous uplift inverts the topographic gradient, with higher elevation in the center (2.2 km) of the model than in the front/back (1.5 km). Besides the major sediment depocenters (exceeding ~6 km in thickness) associated with the major faults, smaller depocenters (~4 km thick) are associated with the conjugate faults.

4. Discussion

4.1. Evolution of Faulting

In all models, two rifts form at the location of the two weak seeds. Models M1 to M5 show variable faulting styles, in particular in terms of fault propagation, development of structures in the rift linkage area, and in the degree of rift segmentation. In the following, we will discuss the sensitivity of fault evolution to notch offset, crustal strength, and erosional efficiency (e.g., Figure 7).

Notch offset is critical for controlling linkage of the propagating major faults. For strong crust, narrow (35 km for model M2; Figure 3) to intermediate notch offsets (70 km for model M1; Figure 2) result in interaction and overlap of the propagating major faults. Two small horsts (M2) or a single large horst (M1) form in the center of
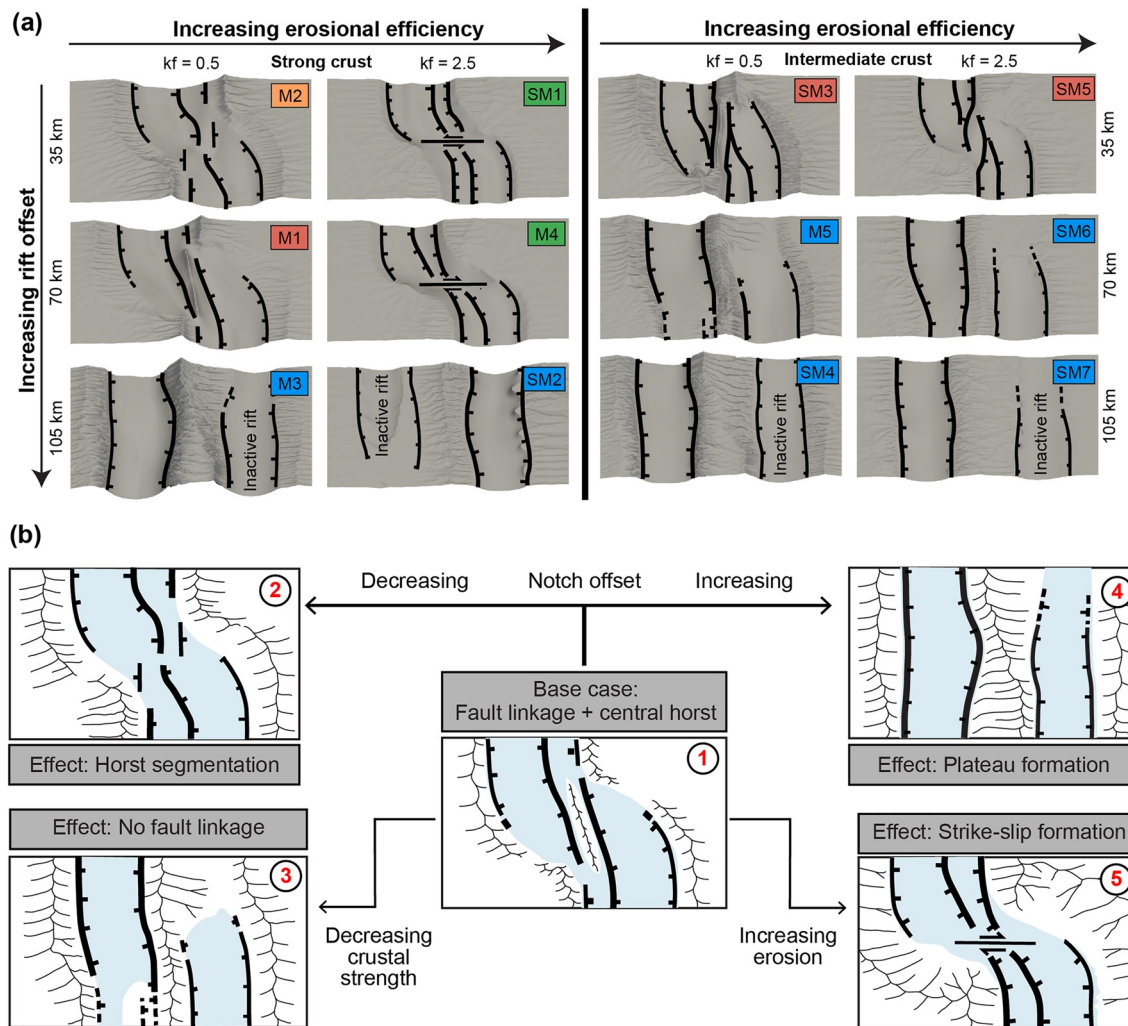
Figure 7. (a) Comparison of characteristic fault patterns and modes of rift linkage and segment interaction for all models at 15 Ma: models with high crustal strength (R1, left) and intermediate crustal strength (R2, right). (1) Cases with fault linkage and horst formation, red label, (2) cases with horst segmentation, orange label, (3) cases with no fault linkage and (4) plateau formation, blue label, and (5) cases with strike slip faulting, green label. Major faults are indicated with thick black lines, minor structures with thin black lines. (b) Cartoons of the effects of varying offset of the weak zone, erosional efficiency, and crustal strength, with respect to the reference case.

the rift. In model M1, localization of deformation on the horst-bounding faults and high uplift rates lead to emergence of the horst and two basins. For M1 and M2, the major fault is segmented, and the segments forming the initial rift shoulders are deactivated. In contrast, increasing notch offset leads to two disconnected rifts without interaction (e.g., Fig. 7a; Fig. 4). Nonetheless, faster propagation of the left rift deactivates the right rift in these cases. Model sensitivity tests, not included here, show that fault interaction is also dependent on along-strike model width. A wider model than ours (250 km wide), can lead to fault and rift interaction for a notch offset larger than investigated here (see e.g., Neuharth et al., 2021).

For a given notch offset (70 km), weaker crust promotes more distributed and symmetric deformation, as a result of the weaker coupling between crust and mantle (Beucher & Huismans, 2020). Overall, the maximum offset on the major boundary faults is reduced while it increases on the conjugate faults resulting in more symmetric individual rift segments, with lower rift shoulders in comparison with reference model M1 with strong crust (∼2.5 km vs. ∼5 km). Major faults do not overlap, interact less, and don't form horsts. Generally, faults propagate farther in a weaker crust. We speculate, that the reduced fault offset is, in that case, compensated by fault propagation. Less coupling between crust and mantle also suppresses segmentation of the major faults. For strong crust, crustal fault segments connect with mantle shear zones (Figure 2).

Erosional efficiency affects faulting through the positive feedback between footwall erosion, hangingwall deposition, and fault offset (e.g., Maniatis et al., 2009; Olive et al., 2014; Theunissen & Huismans, 2019) (Figure 5). Higher erosional efficiency promotes localization of deformation, extends fault activity, and delays or inhibits fault segmentation. The most striking effect of increased erosional efficiency is on the along-strike fault propagation of the major faults. Higher erosion of the uplifting footwall leads to increased fault offset, but decreases the rate of along-strike propagation to the model center, preventing formation of a central horst. Instead, extension in the central part of the model is accommodated by transform zones with strike-slip motion. Supplementary model SM1 with shorter notch offset shows a similar reduced rate of fault propagation with increased erosional efficiency, whereas SM2 with larger offset does not show this effect.

4.2. Characteristic Architecture of Offset Rift Basins

The rift architecture of two offset rift basins is controlled by the ability of the major faults to propagate, interact, and link with each other. We identify five characteristic fault patterns (Figure 7a): (a) fault linkage and horst formation, (b) horst segmentation, (c) no fault linkage, (d) plateau formation, and (e) strike-slip faulting. These fault patterns are specific to initial conditions and model parameters (Figures 7a and 7b).

Efficient fault linkage and central horst formation (1) are promoted by strong coupling between the crust and mantle lithosphere, by intermediate erosional efficiency, and by intermediate notch offset (Figure 7a). Short notch offset results in horst segmentation. Formation of strike-slip faults in the rift linkage area (5) requires high erosional efficiency and is enhanced by low notch offset that promotes linking of the major faults with the conjugates of the opposite rift segment (Figure 7a).

No fault linkage (3) and plateau formation (4) are promoted by less fault interaction. Limited fault interaction primarily results from large offset between rift basins and decoupling of crust and mantle lithosphere. For instance, intermediate crustal strength paired with intermediate notch offset (i.e., 70 km) leads to limited interaction and linkage between the faults, and results in a small continuous horst with overlapping opposite-dip inner faults (3). Large notch offset impedes fault interaction and linkage and leads to two independent rifts separated by an elevated plateau (4). This behavior is independent of crustal rheology and erosional efficiency (Figure 7a). Fault propagation competes between the two rifts, and after one rift has fully propagated through the model domain, the other rift is deactivated.

Together, the different investigated parameters (inherited weakness offset, crustal strength, efficiency of erosion) affect fault interaction between the rifts and the resulting architecture of the offset rift basins in different ways: If inherited weaknesses are widely offset, the individual rift segments will probably not interact. In contrast, if inherited weaknesses are close with low to intermediate offset, fault interaction depends on tectonic and climatic boundary conditions. Strong crust promotes fault interaction and linkage, with strike-slip faults when erosion is very efficient.

4.3. Comparison of Models With Natural Examples

The western branch of the EARS is a good analogue for our model experiments, in particular the central part of the western branch, which extends from the northern end of Lake Tanganyika through Lake Rukwa to the northern end of Lake Malawi (Figure 8). The different lakes correspond to individual rift segments, and the Lake Tanganyika is segmented (e.g., Morley et al., 1990; Macgregor, 2015). Faulting and rifting commenced 9–12 Ma ago at Lake Tanganyika, at the Miocene/Pliocene boundary at Lake Rukwa, and at 4–8 Ma at the northern part of Lake Malawi (Cohen et al., 1993; Macgregor, 2015). We note evidence for older rift initiation of the Rukwa rift documented by Oligocence strata (e.g., Roberts et al., 2012). Offset weak inherited structures are thought to control the localization of deformation and the variation of offset in these rift segments (e.g., Heilman et al., 2019; Kolawole et al., 2018, 2021; Wright et al., 2020). The notch length of 50 km used in our models seems appropriate given that rifting in the EARS is often associated with old structures extending over tens of kilometers.

In this part of the EARS, individual rift segments form asymmetric half grabens. Rift shoulders are 1,000–2,000 m high, in particular in the northern part and on the western side of Lake Tanganyika. Cross-section F/F' through the lake Malawi half-graben (Figure 8), reveals strong asymmetry with significant footwall uplift and sediment
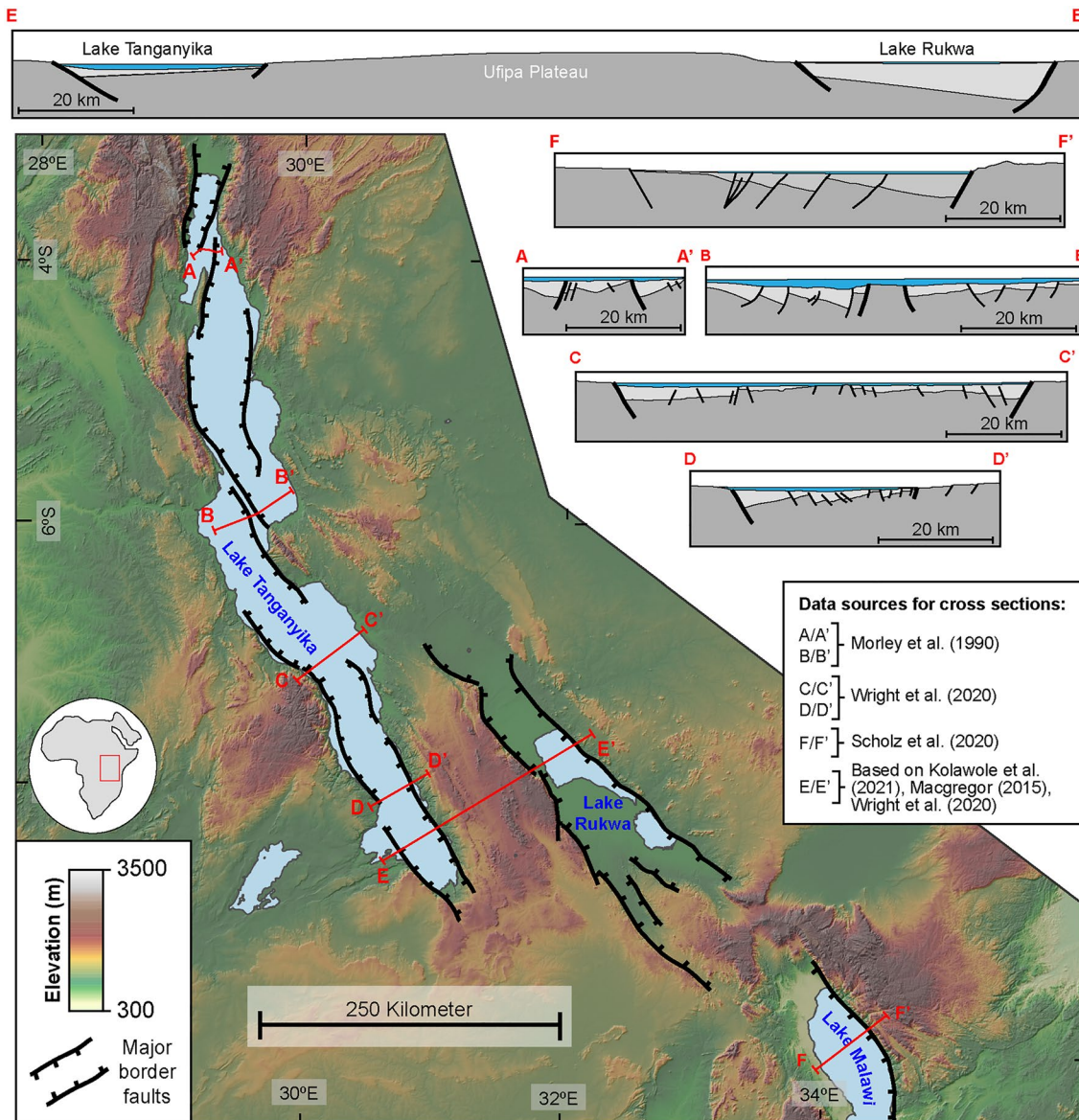
Figure 8. Topographic map of the central portion of the western branch of the East African Rift system. The major basins (Lake Tanganyika, Lake Rukwa, and Lake Malawi) and the major border faults are indicated. Six cross sections through the different rifts are displayed as well. Faults are after Morley et al. (1990); Ebinger (1989); Kolawole et al. (2021).

deposition associated with the border fault. The models show a similar geometry at the location of the notches, especially during the early stages of rifting (Figures 3 and 6).

Cross sections A/A' and B/B' show 10–20 km wide basement horsts below the lake surface, in the transfer zones between rift segments. These structures resemble the patterns of faulting observed in the area of fault overlap of model M1 (Figure 7a).

Profiles C/C' and D/D' illustrate the along-strike variation in rift geometry. At the location of profile C/C', the rift consists of an asymmetric graben with the major border fault on the western side and complex internal geometry of the basin. At the location of profile D/D', the rift evolves to an asymmetric half-graben. The western rift shoulder is lower and offset on the conjugate fault is lower. This is typical of what we observe in the models along-strike the rifts, in particular during the early stages of extension.

Section E/E' extends from the southern end of Lake Tanganyika to Lake Rukwa with the elevated (1,200–2,200 m), 80–100 km wide Ufipa Plateau in between the two separate rift segments. In our models an elevated plateau is characteristic for systems with large offset between inherited weaknesses, leading to limited fault interaction (Pattern 4, Figure 7a). Sediments are thicker in the Rukwa basin (>6 km) than in the southern part of Lake Tanganyika (1–2 km). We observe differing sediment thickness in the basins surrounding the high-elevation plateau in our simulations as well (Figure 4). However, the Rukwa Basin experienced multiple rifting phases: the oldest deposits are of Permo-Triassic age and Neogene deposits are commonly 2–3 km thick with a maximum thickness of Cenozoic deposits of >5 km (Morley et al., 1992; Morley et al., 1999; Macgregor, 2015; Kolawole et al., 2021).

In this area of the EARS, no strike-slip faults linking rift segments are observed. In our simulations, we observe strike-slip faulting (Pattern 2, Figure 7a) only for high erosional efficiency (i.e., if the k_f-value is 2.50×10^{-5}). The thickest Neogene sediments reach 6 km in Lake Tanganyika (Wright et al., 2020), 2–3 km in Lake Rukwa (Kolawole et al., 2021; Macgregor, 2015), and 5–6 km in the northern part of Lake Malawi (Scholz et al., 2020). This is consistent with simulated sediment thicknesses after 10–15 Myr of extension for intermediate erosional efficiency (i.e., a k_f-value of 0.50×10^{-5}), significantly less than for models with high erosional efficiency (>9 km). This indicates that formation of strike-slip faults is limited by the efficiency of erosion in this area.

Extending the analysis further north and/or south along-strike the rift system could introduce the problem of variable extension directions and extension rates along-strike the rift system. This is a further complication, that we have not included in our models but that influences the observed structures. The Afar and Arabia-Somalia regions are other possible targets to compare to 3D numerical models. However, we believe that our current model setup is too simplified to reproduce the rift segment interactions of these, where three rifts with different maturity interact with each other (EARS, Gulf of Aden, Red Sea). Future model work could address this area, using a more sophisticated model setup, but would also require much more constraints on model parameters.

4.4. Comparison With Previous Model Work and Model Limitations

Numerical models have been used in a series of earlier studies investigating continental rifting. 2D models with only a mechanical part elucidate the effect of tectonics (e.g., Richter et al., 2021; Tetreault & Buiter, 2018), whereas coupled 2D models have considered the combined effects of tectonic and surface processes (e.g., Andrés-Martínez et al., 2019; Beucher & Huismans, 2020; Neuharth et al., 2022; Olive et al., 2014; Theunissen & Huismans, 2019; L. Wolf, Huismans, Rouby, et al., 2022). So far studies using 3D models have focused solely on the effects of tectonic boundary conditions on the evolution of rifts (e.g., Allken et al., 2011; Allken et al., 2012; Balázs et al., 2018; Brune et al., 2017; Neuharth et al., 2021). Our coupled 3D model allows simulating the effects of both tectonic boundary and initial conditions and surface processes on the three-dimensional evolution of fault propagation, linkage, and rift architecture.

We corroborate that a weaker rheology (and hence lower crustal strength) results in less strain localization, reduces rift asymmetry, and lowers rift shoulder elevation and fault offset (Beucher & Huismans, 2020). We also observe that reduced crustal strength promotes fault propagation, with less fault interaction between propagating faults (Neuharth et al., 2021). We did not include lateral variations of rheology in our models, which may impact the linkage between faults and rift segments (Brune et al., 2017; Gouiza & Naliboff, 2021). Hence, we can not directly compare our models with natural examples, where lateral variations in crustal strength are documented.

Similar to modeling studies in 2D, we observe in three dimensions that the feedback between footwall erosion and hanging wall deposition leads to increased fault offset (Andrés-Martínez et al., 2019; Maniatis et al., 2009; Neuharth et al., 2022; Olive et al., 2014; Theunissen & Huismans, 2019; L. Wolf, Huismans, Rouby, et al., 2022). In addition, increased erosion extends fault activity and prevents the segmentation of individual faults. In particular, efficient erosion promotes rift linkage by strike-slip faulting in high crustal strength cases (Figure 7). In previous studies this type of rift linkage has often been explained by structural inheritance and by the horizontal distances between the initial strain-weakened notches (Allken et al., 2011, 2012; Neuharth et al., 2021) rather than by the feedback of surface processes on tectonics demonstrated here.

Our model setup considers only two simple, strain-weakened notches with uniform length and we only vary the horizontal offset between the notches (Figure 1). In comparison, other 3D studies use more complicated

3D-geometries for strain inheritance (e.g., Glerum et al., 2020; Heron et al., 2019) or vary the notch length between the models (e.g., Balázs et al., 2018; Neuharth et al., 2021). As shown by Allken et al. (2012); Neuharth et al. (2021), we confirm that the rift architecture and type of linkage is strongly dependent on the horizontal notch offset and crustal strength, and that deactivation of one rift occurs for particularly wide notch offset (our Plateau formation pattern in Figure 7). Although we did not test this with our models, we speculate that notch length would not affect our main conclusions, since rift architecture is not sensitive to notch length (Neuharth et al., 2021).

Our model results should also be viewed with the following limitations in mind: the horizontal model dimension comprises only 500×250 km (Figure 1a). A larger domain allows fault linkage also for wider notch offset (e.g., Neuharth et al., 2021). We did also not test the sensitivity of rift architecture to extension rate and only consider a single, total extension rate of 0.5 cm yr^{-1}. Furthermore, we did not include any spatial or temporal variations in parameters in our models. Testing for instance the effect of spatial variations in erosional efficiency, crustal strength, or extension rate on rift architecture could be a target for future studies that also use a larger model domain.

5. Conclusions

Using a high-resolution 3D thermo-mechanical model coupled with a landscape evolution model, we simulate the lithosphere-scale development and linkage of offset continental rift basins. We investigate how the rift architecture between two propagating rifts is affected by the tectonic situation (crustal strength, offset between inherited structures) and surface processes efficiency. We focus on analyzing fault propagation, fault interaction, and rift linkage. Our observations allow us to draw the following conclusions:

A lower crustal strength allowing for decoupling between upper crust and lithospheric mantle limits the interaction between individual rifts. Inherited structures strongly control fault interaction and rift linkage. If the distance between the inherited structures is too large, no fault interaction occurs. The models show that efficient surface processes lead to a positive feedback between fault offset, footwall erosion, and hanging wall deposition. Furthermore, efficient surface processes decrease fault propagation and fault segmentation. We identify five characteristic patterns of rift architecture that reflect the sensitivity to crustal strength, offset of inherited weaknesses, and surface process efficiency:

1. Fault linkage and formation of a central horst between the propagating rifts occurs for a high crustal strength, intermediate erosional efficiency, and low to intermediate offset between inherited weak zones.
2. Decreasing notch offset leads to segmentation of the central horst.
3. No fault linkage, formation of a continuous central horst, and disconnected rift basins are promoted in case of intermediate crustal strength.
4. In case of large rift offset, fault linkage and rift interaction is prevented, and a wide plateau-like horst is formed between the two rifts, irrespective of crustal strength and erosional efficiency.
5. Very efficient surface processes result in the formation of strike-slip faults between individual offset rift segments, if crustal strength is high.

We identify several of our proposed rift architectures and model observations in the western branch of the EARS. In summary, our study demonstrates, the sensitivity of the 3D evolution of rift systems to both the tectonic and surface process boundary conditions. Further deployment of coupled 3D models could expand the parameter space (e.g., test the sensitivity to extension rate or consider spatial variations in the parameters) and further analyze the evolution of topography and sediments. This will lead to a better understanding of the development of continental rifts.

Data Availability Statement

We use the code pTatin3D (https://bitbucket.org/ptatin/ptatin3d/src/master/) for the thermo-mechanical model, and as earth surface process code we use the code FastScape (https://fastscape.org/). Both codes are applied in a coupled manner as outlined in the manuscript. The data used for the analyses and figures in the paper are available for all models at https://doi.org/10.6084/m9.figshare.19666074.v2 (L. Wolf, Huismans, Wolf, et al., 2022).

References

Allken, V., Huismans, R. S., & Thieulot, C. (2011). Three-dimensional numerical modeling of upper crustal extensional systems. *Journal of Geophysical Research*, *116*(B10), B10409. https://doi.org/10.1029/2011JB008319

Allken, V., Huismans, R. S., & Thieulot, C. (2012). Factors controlling the mode of rift interaction in brittle-ductile coupled systems: A 3D numerical study. *Geochemistry, Geophysics, Geosystems*, *13*, Q05010. https://doi.org/10.1029/2012GC004077

Andrés-Martínez, M., Pérez-Gussinyé, M., Armitage, J., & Morgan, J. P. (2019). Thermomechanical implications of sediment transport for the architecture and evolution of continental rifts and margins. *Tectonics*, *38*(2), 641–665. https://doi.org/10.1029/2018TC005346

Balázs, A., Matenco, L., Vogt, K., Cloetingh, S., & Gerya, T. (2018). Extensional polarity change in continental rifts: Inferences from 3-D numerical modeling and observations. *Journal of Geophysical Research: Solid Earth*, *123*(9), 8073–8094. https://doi.org/10.1029/2018JB015643

Bassi, G., Keen, C. E., & Potter, P. (1993). Contrasting styles of rifting - models and examples from the eastern Canadian margin. *Tectonics*, *12*(3), 639–655. https://doi.org/10.1029/93tc00197

Beaumont, C., Fullsack, P., & Hamilton, J. (1992). Erosional control of active compressional orogens. In K. R. McClay (Ed.), *Thrust tectonics* (pp. 1–18). Springer Netherlands. https://doi.org/10.1007/978-94-011-3066-0_1

Beucher, R., & Huismans, R. S. (2020). Morphotectonic evolution of passive margins undergoing active surface processes: Large-scale experiments using numerical models. *Geochemistry, Geophysics, Geosystems*, *21*(5). https://doi.org/10.1029/2019GC008884

Braun, J., Thieulot, C., Fullsack, P., DeKool, M., Beaumont, C., & Huismans, R. S. (2008). DOUAR: A new three-dimensional creeping flow numerical model for the solution of geological problems. *Physics of the Earth and Planetary Interiors*, *171*(1–4), 76–91. https://doi.org/10.1016/j.pepi.2008.05.003

Braun, J., & Willett, S. D. (2013). A very efficient O(N), implicit and parallel method to solve the stream power equation governing fluvial incision and landscape evolution. *Geomorphology*, *180–181*, 170–179. https://doi.org/10.1016/j.geomorph.2012.10.008

Brune, S., Corti, G., & Ranalli, G. (2017). Controls of inherited lithospheric heterogeneity on rift linkage: Numerical and analog models of interaction between the Kenyan and Ethiopian rifts across the Turkana depression: Rift linkage modeling, Turkana Region. *Tectonics*, *36*(9), 1767–1786. https://doi.org/10.1002/2017TC004739

Buck, W. R. (1991). Modes of continental lithospheric extension. *Journal of Geophysical Research: Solid Earth*, *96*(B12), 20161–20178. https://doi.org/10.1029/91jb01485

Champagnac, J.-D., Molnar, P., Sue, C., & Herman, F. (2012). Tectonics, climate, and mountain topography. *Journal of Geophysical Research*, *117*(B2), a–n. https://doi.org/10.1029/2011JB008348

Cohen, A. S., Soreghan, M. J., & Scholz, C. A. (1993). Estimating the age of formation of lakes: An example from Lake Tanganyika, East African Rift system. *Geology*, *21*(6), 511–514. https://doi.org/10.1130/0091-7613(1993)021<0511:etaofo>2.3.co;2

Corti, G., Molin, P., Sembroni, A., Bastow, I. D., & Keir, D. (2018). Control of pre-rift lithospheric structure on the architecture and evolution of continental rifts: Insights from the main Ethiopian Rift, East Africa. *Tectonics*, *37*(2), 477–496. https://doi.org/10.1002/2017TC004799

Culling, W. E. H. (1963). Soil creep and the development of hillside slopes. *The Journal of Geology*, *71*, 127–161. https://doi.org/10.1086/626891

Duclaux, G., Huismans, R. S., & May, D. A. (2020). Rotation, narrowing, and preferential reactivation of brittle structures during oblique rifting. *Earth and Planetary Science Letters*, *531*, 115952. https://doi.org/10.1016/j.epsl.2019.115952

Dunbar, J. A., & Sawyer, D. S. (1996). Three-dimensional dynamical model of continental rift propagation and margin plateau formation. *Journal of Geophysical Research: Solid Earth*, *101*(B12), 27845–27863. https://doi.org/10.1029/96jb01231

Ebinger, C. J. (1989). Tectonic development of the Western branch of the East African Rift system. *The Geological Society of America Bulletin*, *101*(7), 885–903. https://doi.org/10.1130/0016-7606(1989)101<0885:tdotwb>2.3.co;2

Enkelmann, E., Zeitler, P. K., Pavlis, T. L., Garver, J. I., & Ridgway, K. D. (2009). Intense localized rock uplift and erosion in the St Elias orogen of Alaska. *Nature Geoscience*, *2*(5), 360–363. https://doi.org/10.1038/ngeo502

Erdős, Z., Huismans, R. S., & Van der Beek, P. (2015). First-order control of syntectonic sedimentation on crustal-scale structure of mountain belts. *Journal of Geophysical Research: Solid Earth*, *120*(7), 5362–5377. https://doi.org/10.1002/2014JB011785

Fazlikhani, H., Fossen, H., Gawthorpe, R. L., Faleide, J. I., & Bell, R. E. (2017). Basement structure and its influence on the structural configuration of the northern North Sea Rift: Basement Shear Zones in the Northern North Sea. *Tectonics*, *36*(6), 1151–1177. https://doi.org/10.1002/2017TC004514

Gawthorpe, R. L., & Hurst, J. M. (1993). Transfer zones in extensional basins: Their structural style and influence on drainage development and stratigraphy. *Journal of the Geological Society*, *150*(6), 1137–1152. https://doi.org/10.1144/gsjgs.150.6.1137

Gawthorpe, R. L., & Leeder, M. R. (2000). Tectono-sedimentary evolution of active extensional basins. *Basin Research*, *12*(3–4), 195–218. https://doi.org/10.1111/j.1365-2117.2000.00121.x

Gleason, G. C., & Tullis, J. (1995). A flow law for dislocation creep of quartz aggregates determined with the molten salt cell. *Tectonophysics*, *247*(1), 1–23. https://doi.org/10.1016/0040-1951(95)00011-B

Glerum, A., Brune, S., Stamps, D. S., & Strecker, M. R. (2020). Victoria continental microplate dynamics controlled by the lithospheric strength distribution of the East African Rift. *Nature Communications*, *11*(1), 2881. https://doi.org/10.1038/s41467-020-16176-x

Glotzbach, C., Beek, P. v. d., Carcaillet, J., & Delunel, R. (2013). Deciphering the driving forces of erosion rates on millennial to million-year timescales in glacially impacted landscapes: An example from the Western Alps. *Journal of Geophysical Research: Earth Surface*, *118*(3), 1491–1515. https://doi.org/10.1002/jgrf.20107

Gouiza, M., & Naliboff, J. (2021). Rheological inheritance controls the formation of segmented rifted margins in cratonic lithosphere. *Nature Communications*, *12*(1), 4653. https://doi.org/10.1038/s41467-021-24945-5

Grujic, D., Coutand, I., Bookhagen, B., Bonnet, S., Blythe, A., & Duncan, C. (2006). Climatic forcing of erosion, landscape, and tectonics in the Bhutan Himalayas. *Geology*, *34*(10), 801–804. https://doi.org/10.1130/G22648.1

Heilman, E., Kolawole, F., Atekwana, E. A., & Mayle, M. (2019). Controls of basement fabric on the linkage of rift segments. *Tectonics*, *38*(4), 1337–1366. https://doi.org/10.1029/2018TC005362

Hemelsdaël, R., Ford, M., Malartre, F., & Gawthorpe, R. (2017). Interaction of an antecedent fluvial system with early normal fault growth: Implications for syn-rift stratigraphy, western Corinth Rift (Greece). *Sedimentology*, *64*(7), 1957–1997. https://doi.org/10.1111/sed.12381

Heron, P. J., Peace, A. L., McCaffrey, K. J. W., Welford, J. K., Wilson, R., Hunen, J., & Pysklywec, R. N. (2019). Segmentation of rifts through structural inheritance: Creation of the Davis strait. *Tectonics*, *38*(7), 2411–2430. https://doi.org/10.1029/2019TC005578

Hodgson, D. M., Bernhardt, A., Clare, M. A., Da Silva, A.-C., Fosdick, J. C., Mauz, B., et al. (2018). Grand challenges (and great opportunities) in sedimentology, stratigraphy, and diagenesis research. *Frontiers of Earth Science*, *6*, 173. https://doi.org/10.3389/feart.2018.00173

Huismans, R. S., & Beaumont, C. (2003). Symmetric and asymmetric lithospheric extension: Relative effects of frictional-plastic and viscous strain softening. *Journal of Geophysical Research*, *108*(B10). https://doi.org/10.1029/2002JB002026

Jourdon, A., Le Pourhiet, L., Mouthereau, F., & May, D. (2020). Modes of propagation of continental breakup and associated oblique rift structures. *Journal of Geophysical Research: Solid Earth*, *125*(9). https://doi.org/10.1029/2020JB019906

Karato, S.-i., & Wu, P. (1993). Rheology of the upper mantle: A synthesis. *Science*, *260*(5109), 771–778. https://doi.org/10.1126/science.260.5109.771

Katzman, R., Tenbrink, U. S., & Lin, J. A. (1995). 3-dimensional modeling of pull-apart basins - Implications for the tectonics of the dead-sea basin. *Journal of Geophysical Research: Solid Earth*, *100*(B4), 6295–6312. https://doi.org/10.1029/94jb03101

Kolawole, F., Atekwana, E. A., Laó-Dávila, D. A., Abdelsalam, M. G., Chindandali, P. R., Salima, J., & Kalindekafe, L. (2018). Active deformation of Malawi Rift's North Basin hinge zone modulated by reactivation of preexisting Precambrian shear zone fabric. *Tectonics*, *37*(3), 683–704. https://doi.org/10.1002/2017TC004628

Kolawole, F., Phillips, T. B., Atekwana, E. A., & Jackson, C. A.-L. (2021). Structural inheritance controls strain distribution during early continental rifting, Rukwa Rift. *Frontiers of Earth Science*, *9*, 707–869. https://doi.org/10.3389/feart.2021.707869

Le Pourhiet, L., May, D. A., Huille, L., Watremez, L., & Leroy, S. (2017). A genetic link between transform and hyper-extended margins. *Earth and Planetary Science Letters*, *465*, 184–192. https://doi.org/10.1016/j.epsl.2017.02.043

Macgregor, D. (2015). History of the development of the East African Rift System: A series of interpreted maps through time. *Journal of African Earth Sciences*, *101*, 232–252. https://doi.org/10.1016/j.jafrearsci.2014.09.016

Mackwell, S. J., Zimmerman, M. E., & Kohlstedt, D. L. (1998). High-temperature deformation of dry diabase with application to tectonics on Venus. *Journal of Geophysical Research*, *103*(B1), 975–984. https://doi.org/10.1029/97JB02671

Maniatis, G., Kurfeß, D., Hampel, A., & Heidbach, O. (2009). Slip acceleration on normal faults due to erosion and sedimentation—Results from a new three-dimensional numerical model coupling tectonics and landscape evolution. *Earth and Planetary Science Letters*, *284*(3–4), 570–582. https://doi.org/10.1016/j.epsl.2009.05.024

Manighetti, I., Tapponnier, P., Courtillot, V., Gallet, Y., Jacques, E., & Gillot, P. Y. (2001). Strain transfer between disconnected, propagating rifts in Afar. *Journal of Geophysical Research: Solid Earth*, *106*(B7), 13613–13665. https://doi.org/10.1029/2000jb900454

Manighetti, I., Tapponnier, P., Courtillot, V., Gruszow, S., & Gillot, P. Y. (1997). Propagation of rifting along the Arabia-Somalia plate boundary: The Gulfs of Aden and Tadjoura. *Journal of Geophysical Research: Solid Earth*, *102*(B2), 2681–2710. https://doi.org/10.1029/96jb01185

Manighetti, I., Tapponnier, P., Gillot, P. Y., Jacques, E., Courtillot, V., Armijo, R., et al. (1998). Propagation of rifting along the Arabia-Somalia plate boundary: Into Afar. *Journal of Geophysical Research: Solid Earth*, *103*(B3), 4947–4974. https://doi.org/10.1029/97jb02758

May, D. A., Brown, J., & Pourhiet, L. L. (2014). pTatin3D: High-performance methods for long-term lithospheric dynamics. In *SC14: International conference for high performance computing, networking, storage and analysis* (pp. 274–284). IEEE. https://doi.org/10.1109/SC.2014.28

May, D. A., Brown, J., & Pourhiet, L. L. (2015). A scalable, matrix-free multigrid preconditioner for finite element discretizations of heterogeneous Stokes flow. *Computer Methods in Applied Mechanics and Engineering*, *290*, 496–523. https://doi.org/10.1016/j.cma.2015.03.014

McConnell, R. B. (1972). Geological development of rift system of Eastern Africa. *The Geological Society of America Bulletin*, *83*(9), 2549. https://doi.org/10.1130/0016-7606(1972)83[2549:Gdotrs]2.0.Co;2

Molnar, N., Cruden, A., & Betts, P. (2020). The role of inherited crustal and lithospheric architecture during the evolution of the Red Sea: Insights from three dimensional analogue experiments. *Earth and Planetary Science Letters*, *544*, 116377. https://doi.org/10.1016/j.epsl.2020.116377

Molnar, P., & England, P. (1990). Late Cenozoic uplift of mountain ranges and global climate change: Chicken or egg? *Nature*, *346*(6279), 29–34. https://doi.org/10.1038/346029a0

Morley, C. K. (2002). Evolution of large normal faults: Evidence from seismic reflection data. *AAPG Bulletin*, *86*. https://doi.org/10.1306/61EEDBFC-173E-11D7-8645000102C1865D

Morley, C. K. (2010). Stress re-orientation along zones of weak fabrics in rifts: An explanation for pure extension in 'oblique' rift segments? *Earth and Planetary Science Letters*, *297*(3–4), 667–673. https://doi.org/10.1016/j.epsl.2010.07.022

Morley, C. K., Cunningam, S., Wescott, W., & Harper, R. (1999). Geology and geophysics of the Rukwa Rift. *Geoscience of Rift Systems—Evolution of East Africa*, *44*, 91–110. https://doi.org/10.1306/St44623C5

Morley, C. K., Cunningham, S. M., Harper, R. M., & Wescott, W. A. (1992). Geology and geophysics of the Rukwa Rift, East-Africa. *Tectonics*, *11*(1), 69–81. https://doi.org/10.1029/91tc02102

Morley, C. K., Nelson, R. A., Patton, T. L., & Munn, S. G. (1990). Transfer zones in the East African Rift system and their relevance to hydrocarbon exploration in rifts. *AAPG Bulletin*, *74*(8), 1234–1253. https://doi.org/10.1306/0C9B2475-1710-11D7-8645000102C1865D

Naliboff, J. B., Glerum, A., Brune, S., Péron-Pinvidic, G., & Wrona, T. (2020). Development of 3-D rift heterogeneity through fault network evolution. *Geophysical Research Letters*, *47*(13). https://doi.org/10.1029/2019GL086611

Neuharth, D., Brune, S., Glerum, A., Heine, C., & Welford, J. K. (2021). Formation of continental microplates through rift linkage: Numerical modeling and its application to the flemish cap and Sao Paulo Plateau. *Geochemistry, Geophysics, Geosystems*, *22*(4). https://doi.org/10.1029/2020GC009615

Neuharth, D., Brune, S., Wrona, T., Glerum, A., Braun, J., & Yuan, X. (2022). Evolution of rift systems and their fault networks in response to surface processes. *Tectonics*, *41*(3), e2021TC007166. https://doi.org/10.1029/2021TC007166

Olive, J.-A., Behn, M. D., & Malatesta, L. C. (2014). Modes of extensional faulting controlled by surface processes: Normal faulting and surface processes. *Geophysical Research Letters*, *41*(19), 6725–6733. https://doi.org/10.1002/2014gl061507

Phillips, T. B., Fazlikhani, H., Gawthorpe, R. L., Fossen, H., Jackson, C. A., Bell, R. E., et al. (2019). The influence of structural inheritance and multiphase extension on rift development, the northern North sea. *Tectonics*, *38*(12), 4099–4126. https://doi.org/10.1029/2019TC005756

Richter, M. J. E. A., Brune, S., Riedl, S., Glerum, A., Neuharth, D., & Strecker, M. R. (2021). Controls on asymmetric rift dynamics: Numerical modeling of strain localization and fault evolution in the Kenya Rift. *Tectonics*, *40*(5). https://doi.org/10.1029/2020TC006553

Roberts, E. M., Stevens, N. J., O'Connor, P. M., Dirks, P. H. G. M., Gottfried, M. D., Clyde, W. C., et al. (2012). Initiation of the western branch of the East African Rift coeval with the eastern branch. *Nature Geoscience*, *5*(4), 289–294. https://doi.org/10.1038/Ngeo1432

Rosendahl, B. R. (1987). Architecture of continental rifts with special reference to East Africa. *Annual Review of Earth and Planetary Sciences*, *15*(1), 445–503. https://doi.org/10.1146/annurev.ea.15.050187.002305

Scholz, C. A., Shillington, D. J., Wright, L. J., Accardo, N., Gaherty, J. B., & Chindandali, P. (2020). Intrarift fault fabric, segmentation, and basin evolution of the Lake Malawi (Nyasa) Rift, East Africa. *Geosphere*, *16*(5), 1293–1311. https://doi.org/10.1130/GES02228.1

Stock, J. D., & Montgomery, D. R. (1999). Geologic constraints on bedrock river incision using the stream power law. *Journal of Geophysical Research*, *104*(B3), 4983–4993. https://doi.org/10.1029/98JB02139

Straub, K. M., Duller, R. A., Foreman, B. Z., & Hajek, E. A. (2020). Buffered, incomplete, and shredded: The challenges of reading an imperfect stratigraphic record. *Journal of Geophysical Research: Earth Surface*, *125*(3). https://doi.org/10.1029/2019JF005079

Tetreault, J., & Buiter, S. (2018). The influence of extension rate and crustal rheology on the evolution of passive margins from rifting to break-up. *Tectonophysics*, *746*, 155–172. https://doi.org/10.1016/j.tecto.2017.08.029

Theunissen, T., & Huismans, R. S. (2019). Long-term coupling and feedback between tectonics and surface processes during non-volcanic rifted margin formation. *Journal of Geophysical Research: Solid Earth*, *124*(11), 12323–12347. https://doi.org/10.1029/2018JB017235

Thieulot, C. (2011). FANTOM: Two- and three-dimensional numerical modelling of creeping flows for the solution of geological problems. *Physics of the Earth and Planetary Interiors*, *188*(1–2), 47–68. https://doi.org/10.1016/j.pepi.2011.06.011

Whipple, K. X. (2009). The influence of climate on the tectonic evolution of mountain belts. *Nature Geoscience*, *2*(2), 97–104. https://doi.org/10.1038/ngeo413

Whipple, K. X., & Tucker, G. E. (1999). Dynamics of the stream-power river incision model: Implications for height limits of mountain ranges, landscape response timescales, and research needs. *Journal of Geophysical Research*, *104*(B8), 17661–17674. https://doi.org/10.1029/1999JB900120

Whittaker, A. C. (2012). How do landscapes record tectonics and climate? *Lithosphere*, *4*(2), 160–164. https://doi.org/10.1130/RF.L003.1

Willett, S. D. (1999). Orogeny and orography: The effects of erosion on the structure of mountain belts. *Journal of Geophysical Research*, *104*(B12), 28957–28981. https://doi.org/10.1029/1999JB900248

Wolf, L., Huismans, R. S., Rouby, D., Gawthorpe, R. L., & Wolf, S. G. (2022). Links between faulting, topography, and sediment production during continental rifting: Insights from coupled surface process, thermomechanical modeling. *Journal of Geophysical Research: Solid Earth*, *127*(3), e2021JB023490. https://doi.org/10.1029/2021JB023490

Wolf, L., Huismans, R. S., Wolf, S. G., Rouby, D., & May, D. A. (2022). Data and animations for manuscript by Wolf et al. (2022) entitled: "Evolution of rift architecture and fault linkage during continental rifting: Investigating the effects of tectonics and surface processes using lithosphere-scale 3D coupled numerical models". *Dataset*. https://doi.org/10.6084/m9.figshare.19666074.v2

Wolf, S. G., Huismans, R. S., Braun, J., & Yuan, X. P. (2022). Topography of mountain belts controlled by rheology and surface processes. *Nature*, *606*(7914), 516–521. https://doi.org/10.1038/s41586-022-04700-6

Wolf, S. G., Huismans, R. S., Muñoz, J., Curry, M. E., & Van der Beek, P. (2021). Growth of collisional orogens from small and cold to large and hot—Inferences from geodynamic models. *Journal of Geophysical Research: Solid Earth*, *126*(2). https://doi.org/10.1029/2020JB021168

Wright, L. J. M., Muirhead, J. D., & Scholz, C. A. (2020). Spatiotemporal variations in upper crustal extension across the different basement terranes of the Lake Tanganyika Rift, East Africa. *Tectonics*, *39*(3). https://doi.org/10.1029/2019TC006019

Yuan, X. P., Braun, J., Guerit, L., Rouby, D., & Cordonnier, G. (2019). A new efficient method to solve the stream power law model taking into account sediment deposition. *Journal of Geophysical Research: Earth Surface*, *124*(6), 1346–1365. https://doi.org/10.1029/2018JF004867

Yuan, X. P., Braun, J., Guerit, L., Simon, B., Bovy, B., Rouby, D., et al. (2019). Linking continental erosion to marine sediment transport and deposition: A new implicit and O(N) method for inverse analysis. *Earth and Planetary Science Letters*, *524*, 115728. https://doi.org/10.1016/j.epsl.2019.115728

Zeitler, P. K., Meltzer, A. S., Koons, P. O., Craw, D., Hallet, B., Chamberlain, C. P., et al. (2001). Erosion, Himalayan geodynamics, and the geomorphology of metamorphism. *Geological Society of America Today*, *11*(1), 4–9. https://doi.org/10.1130/1052-5173(2001)011<0004:ehgatg>2.0.co;2